Inorganic Chemistry
Article
pubs.acs.org/IC

New V^{IV}-Based Metal–Organic Framework Having Framework Flexibility and High CO_2 Adsorption Capacity

Ying-Ya Liu,[†] Sarah Couck,[‡] Matthias Vandichel,[§] Maciej Grzywa,[∥] Karen Leus,[†] Shyam Biswas,[†] Dirk Volkmer,[∥] Jorge Gascon,[⊥] Freek Kapteijn,[⊥] Joeri F. M. Denayer,[‡] Michel Waroquier,[§] Veronique Van Speybroeck,[§] and Pascal Van Der Voort*,[†]

[†]COMOC—Center for Ordered Materials, Organometallics and Catalysis, Department of Inorganic and Physical Chemistry, Ghent University, Krijgslaan 281-S3, 9000 Ghent, Belgium

[‡]Department of Chemical Engineering, Vrije Universiteit Brussel, Pleinlaan 2, 1050 Brussels, Belgium

[§]Center for Molecular Modeling, Ghent University, Technologiepark 903, 9052 Zwijnaarde, Belgium

[∥]Solid State and Materials Chemistry, Institute of Physics, Augsburg University, Universitaetsstrasse 1, 86159 Augsburg, Germany

[⊥]Catalysis and Engineering, Delft University of Technology, Julianalaan 136, 2628 BL Delft, The Netherlands

S *Supporting Information*

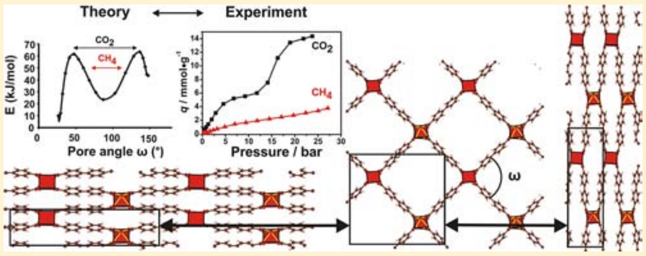

ABSTRACT: A vanadium based metal–organic framework (MOF), VO(BPDC) ($BPDC^{2-}$ = biphenyl-4,4′-dicarboxylate), adopting an expanded MIL-47 structure type, has been synthesized via solvothermal and microwave methods. Its structural and gas/vapor sorption properties have been studied. This compound displays a distinct breathing effect toward certain adsorptives at workable temperatures. The sorption isotherms of CO_2 and CH_4 indicate a different sorption behavior at specific temperatures. In situ synchrotron X-ray powder diffraction measurements and molecular simulations have been utilized to characterize the structural transition. The experimental measurements clearly suggest the existence of both narrow pore and large pore forms. A free energy profile along the pore angle was computationally determined for the empty host framework. Apart from a regular large pore and a regular narrow pore form, an overstretched narrow pore form has also been found. Additionally, a variety of spectroscopic techniques combined with N_2 adsorption/desorption isotherms measured at 77 K demonstrate that the existence of the mixed oxidation states V^{III}/V^{IV} in the titled MOF structure compared to pure V^{IV} increases the difficulty in triggering the flexibility of the framework.

■ INTRODUCTION

Metal–organic frameworks (MOFs) are highly crystalline and porous compounds, which are being intensively studied among other reasons for their potential applications in adsorption and separation technologies and in catalysis.[1] They are built up of metal-oxide clusters or metal ions interconnected by polydentate organic ligands, thus forming two- or three-dimensional porous frameworks. Most of the porous MOFs exhibit a rigid framework under workable conditions and have therefore fixed pore dimensions. However, a few intriguing structures are those whose pore dimensions may change without breaking chemical bonds within the framework, triggered by host–guest interactions at a certain temperature or pressure. This phenomenon has often been termed as "breathing",[2] and the flexible frameworks have been referred to as "dynamic frameworks"[3] or "soft porous crystals".[4]

The best studied example of such flexible coordination compounds is the series of MIL-53, originally developed by Férey's group (MIL stands for Materials of Institute Lavoisier), $M^{III}(OH)(BDC)$ (M^{III} = Al, Cr, Fe, Ga, Sc, and In; BDC^{2-} = 1,4-benzenedicarboxylate).[5] This series of compounds shows a reversible structural change between a large pore (*lp*) form and a narrow pore (*np*) or even a very narrow pore (*vnp*) form upon gas– or solvent–host interactions.[2a,5a,6] This transition is highly dependent on the adsorbate (i.e., CO_2, CH_4, various hydrocarbons, etc.).[1b,7] Furthermore, functionalization of the organic ligand can significantly influence and therefore tune the flexibility of the network.[8] An isostructural analogue of MIL-53 is MIL-47. The main difference between both isostructures lies in the nature of the metal centers and in the presence of −OH groups. Compared to MIL-53, MIL-47 was believed to be relatively rigid. The difference in flexibility between both structures was explained[9] by the presence of −OH groups on M^{III} sites, whereas the V^{IV} has a V═O bond. These −OH groups may strongly interact with different adsorbents, inducing structural transformations. Recently, it was shown that a certain degree of flexibility can be induced in the MIL-47 structure by controlling the oxidation state of the V-centers, going from pure V^{III} to mixed V^{IV}/V^{III} valence states.[9] A very recent

Received: June 23, 2012
Published: December 20, 2012

dx.doi.org/10.1021/ic301338a | *Inorg. Chem.* 2013, 52, 113−120

report[10] demonstrated that a structural change can even be observed in MIL-47(V^{IV}) by applying high external mechanical pressure (180−350 MPa). Such flexible frameworks and a fortiori those with a designable flexibility are very promising candidates for applications including selective storage/separation,[11] molecular sensing,[4,12] and drug delivery.[13] Recently, attempts for a complete elucidation of the underlying mechanisms that trigger the breathing effects of flexible MOFs have been made by several groups.[14]

In this Article, we report on the first MOF bearing a V^{IV}− carboxylate coordination unit exhibiting flexibility under mild conditions. This new MOF denoted as COMOC-2 (COMOC = Center for Ordered Materials, Organometallics and Catalysis, Ghent University) features an extended MIL-47 structure [$V^{IV}O(BPDC)$] ($BPDC^{2-}$ = biphenyl-4,4′-dicarboxylate). Noteworthy, in contrast to this vanadium analogue, an isostructure aluminum biphenyl-4,4′-dicarboxylate, known as DUT-5 (Al(OH)(BPDC), DUT denoted as Dresden University of Technology), showed to be a rigid structure, as demonstrated by the gas (H_2, N_2, CO_2, CH_4) sorption and solvent exchange experiments.[15] Spectroscopic characterization demonstrated that COMOC-2 consists exclusively of V^{IV} centers. It will be referred to as COMOC-2(V^{IV}) hereafter. It shows a distinct breathing effect toward certain adsorptives and exhibits highly selective adsorption of CO_2 over CH_4 at workable temperatures. In situ synchrotron XRD patterns were collected to capture the structure change upon certain gas pressures. Furthermore, the free energy profile was determined along the breathing mode of the empty COMOC-2(V^{IV}) by means of first principles calculations. Two other variants of COMOC-2(V^{IV}) were obtained by slight variation of the reaction parameters: one is in a mixed valence V^{IV}/V^{III} state labeled as COMOC-2(V^{IV}/V^{III}), the other displays a pure large pore phase labeled as COMOC-2(*lp*). Because of the difference in oxidation states, COMOC-2(V^{IV}/V^{III}) shows a different adsorption behavior compared to COMOC-2(V^{IV}). The crystal structure of the large pore phase of COMOC-2 has been determined by Rietveld refinement from the powder XRD data of COMOC-2(*lp*).

■ EXPERIMENTAL SECTION

Materials and General Methods. All starting materials were commercially available reagents of analytical grade and used without further purification. Microwave-assisted syntheses were carried out on a microwave synthesizer (Discover, CEM Inc.). Fourier transform-infrared (FT-IR) spectra were recorded in the region of 400−4000 cm^{-1} on a Bruker EQUINOX 55 FT-IR spectrometer. Diffuse-reflectance infrared Fourier transform (DRIFT) spectra were recorded on a Thermo Nicolet 6700 FT-IR spectrometer, equipped with a nitrogen-cooled MCT detector and a KBr beam splitter. The in situ DRIFT cell was connected to a vacuum manifold and a controlled gas inlet system. Each spectrum was recorded at 120 °C under vacuum. Raman spectra were collected with the RXN1 Raman spectrometer (Kaiser Optical Systems) fitted with a 532 nm laser operating at 40 mW using an optical probe. Elemental analyses were carried out on a Thermo Scientific Flash 2000 CHNS-O Analyzer. Thermogravimetric analysis (TGA) on COMOC-2 was performed with a Netzsch STA 449 F3 Jupiter-simultaneous TG-DSC analyzer in the temperature range of 25−700 °C under nitrogen atmosphere at a heating rate of 10 °C min^{-1}. Laboratory X-ray powder diffraction (XRPD) patterns were recorded on a Seifert XRD 3003 TT diffractometer outfitted with a Meteor 1D detector (for Rietveld Refinement of COMOC-2) or a Thermo Scientific ARL X'Tra diffractometer (for all other compounds), both operated at 40 kV, 40 mA using Cu−Kα (λ = 1.5406 Å). Temperature programmed XRPD (TP-XRPD) patterns were collected on a Bruker D8 Discover X-ray diffractometer equipped with a linear detector using Cu−Kα radiation; the XRD patterns were recorded from room temperature to 620 °C at a heating rate of 0.2 °C s^{-1} under helium atmosphere. The X-ray photoelectron spectroscopy (XPS) measurements were recorded on a Kratos AXIS Ultra spectrometer, equipped with a monochromatic X-ray source and a delay-line detector (DLD). Spectra were obtained using the aluminum anode (Al Kα = 1486.6 eV) operating at 150 W. Analysis of XPS data was performed using the XPSPEAK 4.1 program, using the Shirley function to subtract the background.

Syntheses. *1. Synthesis of COMOC-2-as ([VO(BPDC)] $(DMF)_{0.1}(H_2O)_{0.5}$). a. Method 1: Solvothermal Synthesis.* In total, 0.5 g of $VOSO_4 \cdot H_2O$ and 1.02 g of 4,4′-biphenyldicarboxylic acid (H_2BPDC) were added into 70 mL of DMF. The mixture was transferred to a 100 mL round-bottom flask equipped with a magnetic stirrer. The flask was sealed, heated slowly to 147 °C under stirring, and kept at this temperature for 15−20 h. After completion of the reaction, a yellowish green powder was collected over a membrane filter, washed thoroughly first with DMF, then with methanol to remove the green vanadium impurities, and finally with acetone, and subsequently dried at room temperature under vacuum. Yield, 0.31 g; 34.7%, based on vanadium. Elemental analysis for $[VO(C_{14}H_8O_4)](C_3H_7NO)_{0.1}\,(H_2O)_{0.5}$: calcd, C, 53.1; H, 3.02; N, 0.43 (%); found, C, 53.75; H, 2.97; N, 0.28 (%).

b. Method 2: Microwave-Assisted Synthesis. In total, 0.05 g of $VOSO_4 \cdot H_2O$ and 0.102 g of H_2BPDC were added into 3 mL of DMF and heated to 150 °C under microwave irradiation for 20 min with magnetic stirring. The maximum irradiation power was set to 150 W, with the "powermax" active (air cooling was used during the irradiation). After completion of the reaction, a yellowish green powder was collected over a membrane filter, washed thoroughly first with DMF, then with methanol to remove the green vanadium impurities, and finally with acetone and subsequently dried at room temperature under vacuum. Yield: 0.015 g, 16.8%; based on vanadium. ***Important!*** *COMOC-2 is sensitive to air and moisture and should be stored under an argon atmosphere.*

c. Activation of COMOC-2-as. The COMOC-2-as compound was activated by heating up the sample at a heating rate of 1 °C min^{-1} under vacuum up to 120 °C and held at this temperature for 3 h. This activation temperature was optimized based on the results of nitrogen sorption experiments and powder XRD data.

2. Syntheses of COMOC-2(V^{IV}/V^{III})-as and COMOC-2(lp)-as. COMOC-2(V^{IV}/V^{III})-as can be obtained by a slight variation of the solvothermal reaction parameters described above for COMOC-2-as. The compound was synthesized by prolongation of the reaction time to 24 h or by increasing the reaction temperature to 160 °C. Probably the decomposition products of DMF partially reduce V^{IV} to V^{III}, producing the mixed-valence COMOC-2(V^{IV}/V^{III})-as. In a typical reaction, 0.5 g of $VOSO_4 \cdot H_2O$ and 1.02 g of 4,4′-biphenyldicarboxylic acid (H_2BPDC) were added into 70 mL of DMF. The mixture was transferred to a 100 mL round-bottom flask equipped with a magnetic stirrer. The flask was sealed, heated to 150 °C with a heating rate of ~1 °C min^{-1} under stirring and kept at this temperature for 22 h. After cooling to room temperature, a yellowish green powder was collected over a membrane filter, washed thoroughly first with DMF, then with methanol to remove the green vanadium impurities, and finally with acetone and subsequently dried at room temperature under vacuum.

Moreover, the use of a more concentrated reaction mixture (50 mL of DMF instead of 70 mL) with all other solvothermal reaction parameters unaltered results in the formation the COMOC-2(*lp*)-as, which contains a small amount of free linker, as evidenced by elemental analysis on activated COMOC-2(*lp*) sample: $[VO(C_{14}H_8O_4)](C_3H_7NO)_{0.05}\,(C_{14}H_{10}O_4)_{0.07}$: calcd, C, 55.44; H, 2.78; N, 0.21 (%); found, C, 55.36; H, 2.78; N, 0.23 (%).

XRPD Data Collection and Rietveld Refinement for COMOC-2. For the determination of crystal structure of COMOC-2 from XRPD data, a microcrystalline sample was ground using an agate mortar and pestle and was deposited in the hollow of a zero-background sample holder. Diffraction data were collected at room temperature in the 2θ range of 4.5−90° with 0.02° steps, with a scan speed of 1000 s $step^{-1}$ using a Seifert XRD 3003 TT diffractometer equipped with a Meteor 1D detector, operated at 40 kV, 40 mA for Cu target ($\lambda = 1.5418$ Å). The structure of Al(OH)(BPDC)[15] was used as a model for refinement of the crystal structure. Lattice parameters were determined using the PROSZKI package.[16] The Rietveld refinement was carried out using the Jana2006 program.[17] Weak geometric restraints on bond distances were used during the refinement process. The preferred orientation was refined applying the March−Dollase formula. The preferred orientation was chosen along the [101] direction. After calculation of the difference Fourier maps, no additional peaks were detected, which could be ascribed to the small amount (according to the elemental analysis data) of occluded free linker. The crystal data and details of refinement, atomic coordinates, and bond distances for COMOC-2 are listed in Tables S1, S2 and S3 in the Supporting Information, respectively. The Rietveld refinement plot is shown in Figure S3 in the Supporting Information.

Measurement of Gas and Vapor Sorption Isotherms. Prior to the sorption measurements, the samples were outgassed at 353 K. N_2 sorption experiments were carried out with a Belsorp Mini (Bel Japan, Inc.) apparatus. Equilibrium isotherms of CO_2 and CH_4 were measured using the static volumetric method with an HPA-100 device from VTI Corporation. The vapor phase isotherm of hexane was measured with the gravimetric method on a microbalance of VTI Corporation.

Synchrotron X-ray Powder Diffraction Measurements and Analysis. In situ synchrotron powder diffraction patterns were collected at the Swiss Norwegian beamline (station BM01A) of the European Synchrotron Radiation Facility (Grenoble, France) using an MAR345 image plate detector and a monochromatic beam with a wavelength of 0.752 76 Å. The sample-to-detector distance was 400 mm, and parameters of the detector were calibrated using a silica standard sample. The diffraction patterns were integrated by Fit2D software.[18] The well-ground powder sample was filled in a 0.4 mm glass capillary. A gas dosing system was used to admit CO_2 from vacuum to 17.5 bar of pressure into the capillary filled with sample and exposed to the X-ray beam. Prior to the measurement, the sample was degassed at 80 °C for 30 min (heating rate, 2 °C min^{-1}) under vacuum. The in situ XRPD data upon CO_2 dosing was collected at −40 °C. The temperature was controlled by an Oxford Cryostream Cooler. A typical data set at each pressure point was collected. The XRPD patterns of COMOC-2 under CO_2 pressure of 7.5 and 15 bar were selected for the determination of lattice parameters of the *np* and *lp* phases, respectively. The lattice parameters were determined using the DICVOL program[19] and refined using the STOE's WinXPow[20] software package.

First-Principles Calculations: Methodology. To further unravel the mechanism inducing the breathing, the free energy profile along the breathing mode of the empty COMOC-2(V^{IV}) is computed by means of first principles calculations. For MIL-53, Walker et al. showed that a subtle interplay between dispersion forces and entropic factors controlled the inherent bistable behavior of the material.[21] Along the same line, Stavitski et al. used dispersion corrected first principles calculations to describe the breathing in the amine modified MIL-53(Al) framework.[22] Very recently, Triguero et al. presented a stochastic model of "breathing" transitions in MIL-53. They concluded that (at the level of the crystal) these transformations occur via layer-by-layer shear.[23]

Periodic DFT-D calculations on the entire COMOC-2(V^{IV}) unit cell containing 112 atoms were carried out in the Vienna Ab Initio Simulation Package (VASP 5.2.11),[24] using the PBE exchange-correlation functional[25] and a plane-wave basis set with a general kinetic energy cutoff of 700 eV. The projector augmented wave approximation (PAW)[26] was used. Brillouin zone sampling was restricted to the Γ-point. Gaussian smearing[24b] was applied to improve convergence: 0.05 eV for cell optimizations, 0.02 eV for the subsequent geometry and frequency calculations. Furthermore, D2 van der Waals corrections[27] for the PBE functional are used throughout the optimization, as implemented in the VASP 5.2.11.

First, the most stable open and closed structures are determined using the climbing nudged elastic band (cNEB) methodology[28] with a varying unit cell between constructed cell optimized structures. Then the minima of the narrow pore (*np*) and large pore (*lp*) shape were selected and submitted to a cell optimization. By swapping/switching the two unit cell vectors, an overstretched narrow pore (*np′*) form was constructed. For the cell optimizations, the convergence criterion for the electronic self-consistent field (SCF) problem is set to 10^{-6} eV, while the force convergence criterion is put to 0.01 eV/Å. Between the minimum energy structures, a very detailed climbing NEB-run has been performed.[28] The intermediate points were cell optimized, until the force convergence criterion of 0.02 eV/Å was reached. In this way, an electronic energy profile could be constructed between the three observed phases. Electronic barriers between the phases could be estimated, based on this profile.

In order to get free-energy differences between these forms, frequency calculations have been performed on the various intermediate structures, in order to estimate the zero point vibrational energy and a part of the entropy. To avoid imaginary frequencies, the structures were submitted to tighter convergence criteria, using the unit cell parameters for the previous cell optimization. The general kinetic energy cutoff is lowered to 600 eV for those tight optimizations. The convergence criterion for the electronic self-consistent field (SCF) problem is set to 10^{-7} eV while the force convergence criterion is put to either 0.001 or 0.002 eV/Å. Displacements of ±0.015 Å in the *a*, *b*, and *c*-axis are used in the subsequent Hessian calculation, while the vibrational modes are extracted using the normal-mode analysis as implemented in the in-house developed postprocessing toolkit TAMKIN.[29]

■ RESULTS AND DISCUSSION

Synthesis and Structural Characterization. COMOC-2 can be synthesized solvothermally and under microwave irradiation. The material is thermally stable up to 350 °C, as verified by thermogravimetric analysis (TGA) (Figure S1 in the Supporting Information) and temperature programmed X-ray powder diffraction (TP-XRD) measurements (Figure S2 in the Supporting Information). In COMOC-2(V^{IV}), the vanadium is exclusively V^{IV}, as verified by the ν(V═O) bands observed at 898 cm^{-1} from the Raman spectrum and the absence of ν(OH) bands in the DRIFT spectrum (Figures 1 and 2). However, by varying the reaction conditions, two other variants of

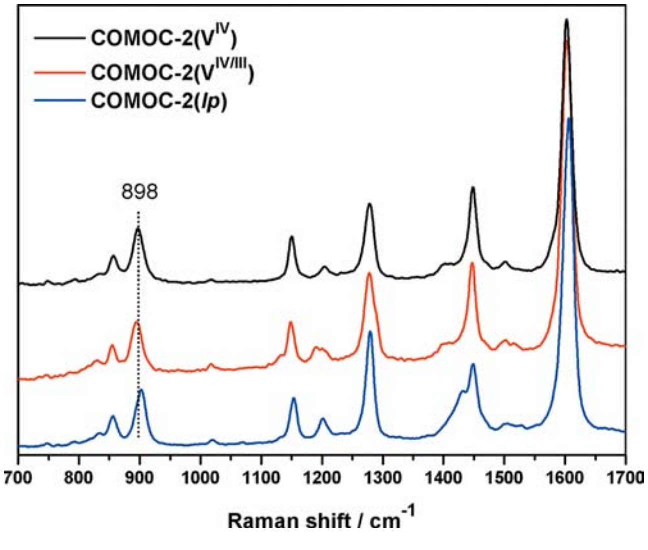

Figure 1. Raman spectra of COMOC-2(V^{IV}), COMOC-2(V^{IV}/V^{III}), and COMOC-2(*lp*). The band centered at 898 cm^{-1}, observed for COMOC-2 and its variants, is assigned to the ν (V═O) mode of the asymmetric V−O−V bond formed by sharing of two consecutive VO_6 octahedra.

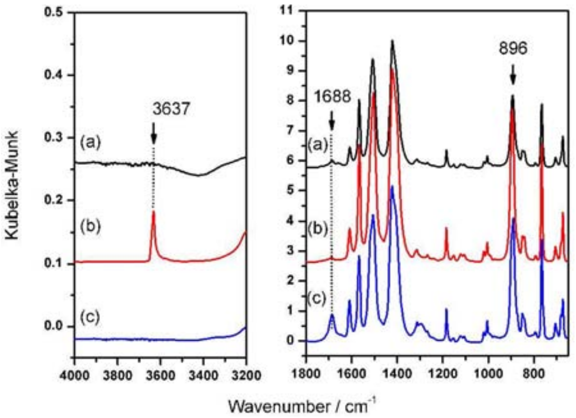

Figure 2. Comparison among the DRIFT spectra of (a) COMOC-2(V^{IV}), (b) COMOC-2(V^{IV}/V^{III}), and (c) COMOC-2(*lp*). The band centered at 896 cm^{-1}, observed for COMOC-2 and its variants, is assigned to the ν (V=O) mode of the asymmetric V−O−V bond formed by sharing of two consecutive VO_6 octahedra. The band at 1688 cm^{-1} is assigned to the stretching vibration of the −COOH group of the free linker. The latter is clearly observed in the IR spectrum of COMOC-2(*lp*) A weak band at 3637 cm^{-1} which is assigned to the ν (OH) from V^{III}−OH, this has only been observed from COMOC-2(V^{IV}/V^{III}).

COMOC-2 were obtained. The V^{III} on COMOC-2(V^{IV}/V^{III}) was evidenced by a weak band at 3637 cm^{-1} which is assigned to the ν(OH) from V^{III}−OH. COMOC-2(*lp*) is in the V^{IV} state but still contains a small amount of free linker in the porous structure (not detectable by means of powder diffraction).

The oxidation state of the vanadium sites was further verified by XPS measurements. The spectra for COMOC-2(*lp*), COMOC-2(V^{IV}) and COMOC-2(V^{IV}/V^{III}) samples are shown in Figure S4 in the Supporting Information. These spectra further confirm that COMOC-2(*lp*) and COMOC-2(V^{IV}) contain exclusively V^{IV}-sites, whereas the COMOC-2(V^{IV}/V^{III}) indeed shows a mixed valence.

COMOC-2(V^{IV}) and COMOC-2(V^{IV}/V^{III}) always show a mixture of *lp* and *np* phase as compared to COMOC-2(*lp*) in powder XRD measurements (Figure S5 in the Supporting Information). It should be mentioned that COMOC-2(V^{IV}/V^{III}) and COMOC-2(*lp*) are two extreme variants synthesized under poorly reproducible conditions. The attempts to realize a more precise control over the ratio of the oxidation state were not successful. COMOC-2(V^{IV}) is the main focus of this Article.

A Rietveld refinement was performed on COMOC-2(*lp*) (Figure S3 in the Supporting Information). The XRD pattern shows that COMOC-2(*lp*) is isostructural with the rigid microporous aluminum biphenyl-4,4′-dicarboxylate DUT-5.[15] COMOC-2 structure (Figure 3) contains chains of octahedra cross-linked by $BPDC^{2-}$ organic linkers. The octahedral chains have a −O=V−O=V− coordination mode. The equatorial corners of the $\{VO_6\}$ octahedra are shared with $BPDC^{2-}$ ligands. The 1D orthorhombic channels parallel to the octahedral chains have an aperture of ∼18.9 Å × 19.4 Å. The refined *lp* structure has an accessible pore volume of 68.2% (2092.7 $Å^3$ per 3068.6 $Å^3$), as calculated by PLATON.[30]

To study the role of oxidation state in determining the extent of framework flexibility, the N_2 adsorption/desorption isotherms (Figure 4) of COMOC-2(V^{IV}) and COMOC-2(V^{IV}/V^{III}) at 77 K were measured and compared. Both samples reveal a two-step sorption behavior, typical for flexible MOFs. For COMOC-2(V^{IV}), a gradual adsorption occurs until P/P_0 = 0.5, when the isotherm reaches its first plateau. Then a very strong uptake of N_2 can be observed, rising steeply in the area P/P_0 = 0.5−1.0; leading to a final uptake volume of 510 cm^3/g at P/P_0 = 0.98 (The maximum N_2 uptake volume of COMOC-2(V^{IV}) with different batches is around 510 ± 40 cm^3/g). This sorption amount is similar to that of DUT-5, which has a Langmuir surface area of about 2335 $m^2\ g^{-1}$ and a total N_2 sorption amount of ∼600 $cm^3\ g^{-1}$. A hysteresis occurs upon desorption. For COMOC-2(V^{IV}/V^{III}), the N_2 sorption isotherms at 77 K also reveal a two-step sorption behavior. However, the first plateau is maintained until P/P_0 = 0.6, then followed by a large nitrogen uptake at higher relative pressures, leading to almost the same sorption amount as for COMOC-2(V^{IV}) at P/P_0 = 0.98. It is interesting to note that the presence of V^{III} in COMOC-2(V^{IV}/V^{III}) compared to pure COMOC-2(V^{IV}) increases the difficulty in triggering the flexibility of the framework. This phenomenon is contrary to MIL-47, in which the presence of V^{IV} centers inhibits the flexibility to a large extent.[31] The reason that COMOC-2(V^{III}/V^{IV}) needs a higher nitrogen pressure to open up the pores might be due to remaining internal stabilization effects (e.g., H-bonding).

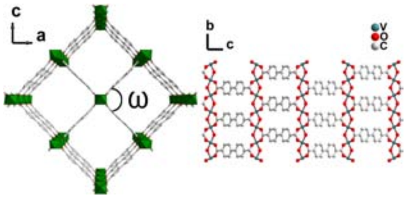

Figure 3. The *lp* form of the COMOC-2 structure (left). The chains of corner-sharing $\{VO_6\}$ octahedra (right). The pore angle ω corresponds to the dihedral angle between the two phenyl rings (left) and is defined according to to $\omega/2 = c/a$.

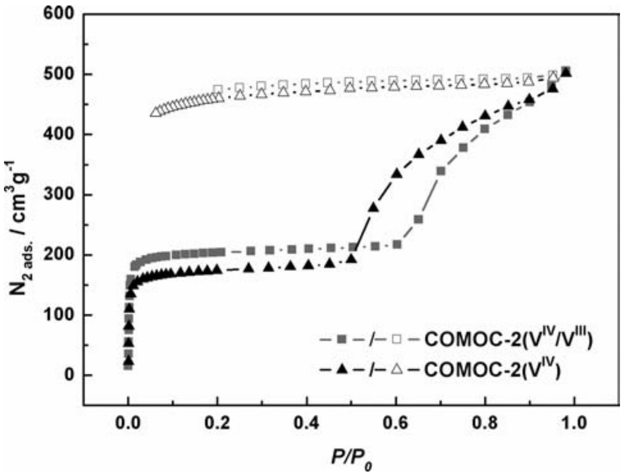

Figure 4. N_2 adsorption (solid symbols) and desorption (open symbols) isotherms of COMOC-2(V^{IV}) (black) and COMOC-2(V^{IV}/V^{III}) (gray) at 77 K.

Gas/Vapor Sorption Isotherms. To further verify the structural transformation of COMOC-2(V^{IV}), CO_2, CH_4, and *n*-hexane sorption isotherms were measured. As shown in Figure 5a, the adsorption isotherms at 303 K for both CO_2 and CH_4 show a classical type I shape, with a capacity of 4.8 mmol of $CO_2\ g^{-1}$ at 25 bar and 1.4 mmol $CH_4\ g^{-1}$ at 27 bar. At 265 K, however, the CO_2 and CH_4 isotherms become distinctively different. In the CO_2 sorption isotherm at around 12.5 bar, a

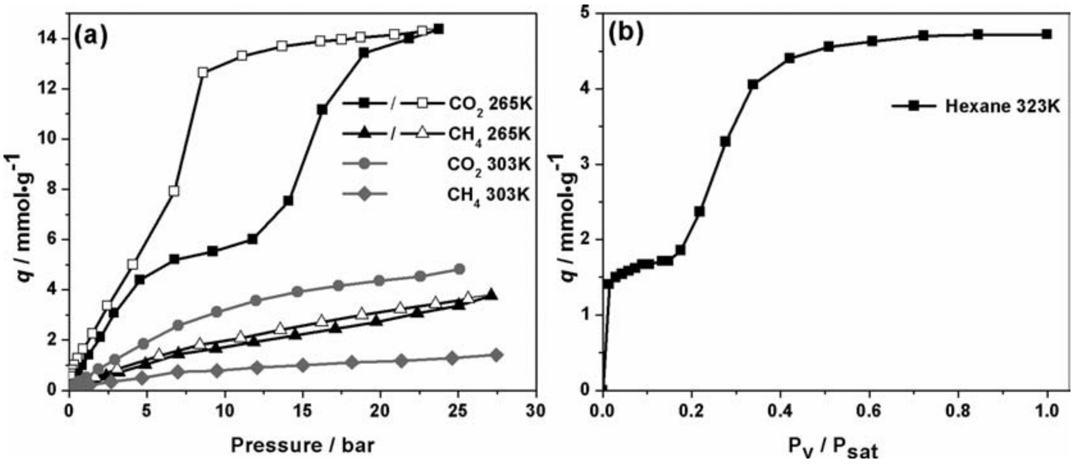

Figure 5. (a) Adsorption (solid symbol) isotherms of COMOC-2(V^{IV}) for CO_2 and CH_4 at 303 and 265 K. Desorption isotherms (open symbol) of CO_2 and CH_4 at 265 K are also included. (b) Adsorption isotherm for *n*-hexane at 323 K on COMOC-2(V^{IV}).

sudden increase in adsorption is observed, reaching 14 mmol g^{-1} at 28 bar, corresponding to almost complete pore filling based on the nitrogen porosimetry data. Two distinct steps are clearly observed, revealing a breathing of the framework. Desorption occurs with a large hysteresis loop. This loop is explained with the stress model developed by Neimark et al.[32] According to this model, structural transition or phase transformation, i.e., the breathing effect, occurs when a certain critical stress threshold is reached. As a consequence, the structural transition pressure depends on the stress threshold. As the stress threshold is different for the various phases, a hysteresis occurs in the adsorption−desorption process. Also at this lower temperature, CH_4 presents a type I isotherm. The desorption curve for CH_4 almost coincides with an adsorption isotherm without the occurrence of any hysteresis. The adsorption profile of COMOC-2(V^{IV}) shows a distinctive adsorption step at 265 K for CO_2 but not for CH_4. This is similar to the CO_2 and CH_4 adsorption behavior of MIL-53 at 304 K.[7]

n-Hexane, having larger molecular weight and thus comparatively larger van der Waals interactions, shows the two-step adsorption behavior associated with framework breathing at 323 K. As shown in Figure 5b, in the first plateau, when COMOC-2(V^{IV}) is in the *np* form, the adsorption capacity is ~2 mmol g^{-1}. The framework opens up at P/P_0 = 0.2 to reach a final hexane adsorption capacity of 4.7 mmol g^{-1} or almost 40 wt % at the saturation pressure.

Analysis of in Situ Synchrotron XRD Patterns. In order to correlate this intriguing breathing adsorption behavior to structural changes in the COMOC-2(V^{IV}) sample, we have performed in situ synchrotron XRD studies at 233 K using the Swiss−Norwegian beamline at the European Synchrotron Radiation Facility (ESRF) equipped with a pressure controlled apparatus dosing CO_2 gas up to a pressure of 17.5 bar. In Figure 6 and Figure S6 in the Supporting Information we show this series of in situ XRPD patterns in a different view. The XRD patterns collected as a function of the CO_2 pressure clearly show the reversible structural changes that accompany the breathing effect. The first XRD pattern of the sample recorded in vacuum shows mainly a *lp* phase, with a fraction of *np* phase. When the pressure is increased up to 1 bar of CO_2, the *lp* to *np* transition occurs immediately, as shown by the sudden decrease in intensity of the *lp* reflections and the appearance of the *np* reflections. The *lp* to *np* transformation process continues until the CO_2 pressure reaches 7.5 bar. Above this pressure, the structure opens again, accompanied by the reversible intensity change in the representative *np* to *lp* reflection peaks. After the high pressure measurements, upon removal of CO_2, the final degassed sample shows peaks entirely consistent with the original phase, confirming the reversibility of this transition process. As shown in Figure S6 (top) in the Supporting Information, the background intensity increases with the amount of CO_2 molecules adsorbed, due to the increment of the electron density when pressure rises.

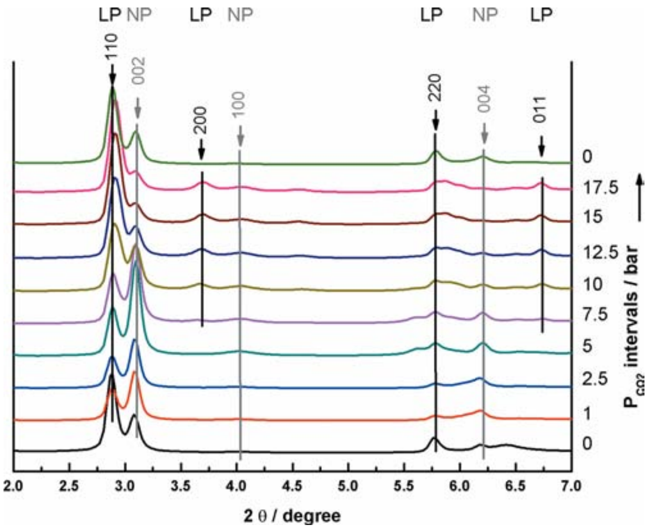

Figure 6. In situ synchrotron XRD patterns of COMOC-2(V^{IV}) (λ = 0.752 76 Å) in the 2θ range 2−7° measured at a certain CO_2 pressure at 233 K. The apparent phase changes and peak indices are marked with arrows.

Since all the in situ synchrotron XRD patterns contain both *lp* and *np* phases, we were unable to select a pattern of pure phase for Rietveld refinement. To estimate the flexibility of the framework, two XRD patterns were selected and used to index the unit cell parameters (Table 1). The *np* phase was indexed to a monoclinic cell with $V \sim 1979$ Å^3, whereas the *lp* phase was indexed to a orthorhombic cell with $V \sim 2956$ Å^3. For comparison, also the lattice parameters determined from theoretical calculations and laboratory XRPD patterns are taken up in Table 1. However, we should stress that the

Table 1. Calculated and Empirically Determined Lattice Parameters for the Different Forms of COMOC-2(V^{IV})

phase	crystal system	a (Å)	b (Å)	c (Å)	α (deg)	β (deg)	γ (deg)	V(Å^3)
np (exptl)[a]	monoclinic	6.651(4)	27.94(4)	10.735(13)	97.06(8)	90	90	1979.4(47)
np (calcd)	orthorhombic	6.991	28.111	6.809	90	90	90	1338.13
lp (exptl)[b]	orthorhombic	6.776(3)	23.087(19)	18.897(9)	90	90	90	2956.1(32)
lp (calcd)	orthorhombic	6.927	21.642	20.498	90	90	90	3073.00
lp (exptl)[c]	orthorhombic	6.957(4)	21.443(3)	20.570(2)	90	90	90	3069(5)
np′ (calcd)	orthorhombic	6.981	7.946	27.275	90	90	90	1512.97

[a] Determined based on synchrotron XRPD pattern with 7.5 bar CO_2 pressure at 233 K. [b] Determined based on synchrotron XRPD pattern with 15 bar CO_2 pressure at 233 K. [c] Crystal data obtained from Rietveld structure refinement on laboratory XRPD pattern of COMOC-2(*lp*) at 293 K.

theoretical predictions for the lattice parameters are based on an empty host system, while the experimental values are resulting from synchrotron XRD patterns under a certain CO_2 pressure. We must be very careful when comparing both results. Because of the adsorption of CO_2 molecules in the structure, the free energy profile can change significantly, especially in the region of the narrow pore phases. The minima around 27° and 148° coresponding, respectively, with *np* and *np*′, as observed in Figure 7, can never be reached as the presence of guest molecules in the pores will obviously lead to larger pore angles. However, when we compare the experimental data recorded at ambient conditions (COMOC-2(*lp*)) with the theoretical *lp* predictions, the data match perfectly.

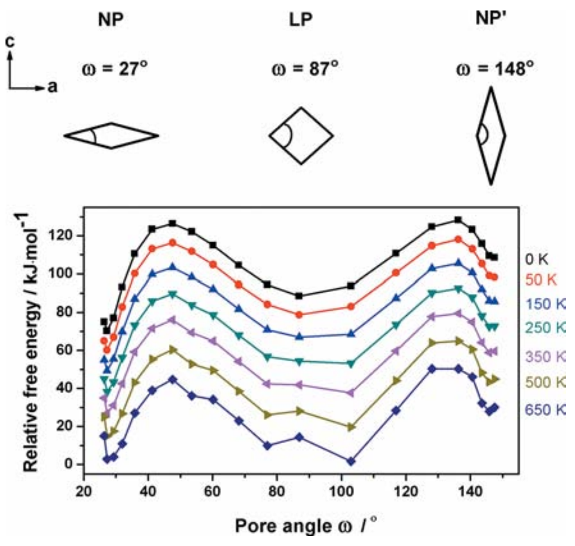

Figure 7. Modeled free energy profiles as a function of temperature for the empty COMOC-2(V^{IV}). Three different minima are observed, representing the different pore shapes: *np*, *lp*, and *np*′. Profiles at different temperatures are shifted by 10 kJ/mol.

Full Free Energy Profile for the Empty COMOC-2(V^{IV}) Structure. Following the methodology, as oulined before, a full free energy profile has been constructed for the empty COMOC-2(V^{IV}) structure in function of the breathing angle ω. As indicated in Figure 7, three stable minima were found in the empty host framework: the *np*, the *lp*, and an overstretched narrow pore (*np*′) form. The two modeled narrow pore forms are different in geometry, displayed in Figures S8–S9 in the Supporting Information, and their unit cell topology may be compared with the *vnp* structure as observed in anhydrous MIL-53(Fe) by the group of Férey,[33] as the theoretical models have been modeled in the complete absence of water. The pore angles for the different structures are shown in Table 2. As only indexed lattice parameters are provided from the synchrotron XRD experiments, a unified force field (UFF) is used to generate structures for the *np* and *lp* phases which fit the experimental XRPD patterns with the cell parameters *a*, *b*, *c* and the angles α, β, and γ as degrees of freedom. Please note that a direct one-to-one correspondence with the ab initio determined lattice parameters should be considered with care, since the XRPD patterns have been measured with the presence of CO_2 adsorbate molecules, while the periodic VASP calculations have been performed in the empty host. As shown in Table 2, all theoretical phases are found to be orthorhombic. The small pore angle for the *np* phase requires some additional clarification. The angle $O_{ca,1}-V-O_{ca,3}$ (α) is more or less constant in the two models (ab initio and empirical) around 85°, which is realistic, and thus plays no significant role in shrinking of the pore angle. The dihedral motion $V-O_{ca}-C_{ca}-C_{pc}$ (χ) determines the rotation of the linker about the $O_{ca}-O_{ca}$ axes of the carboxyl groups. This rotation enables shrinkage or expansion of the entire unit cell. The dihedral angle $O_{ca}-C_{ca}-C_{pc}-C_{ph}$ controls the tilting of the plane of the linker (see Figure S8 in the Supporting Information). Table 2 also reports the average χ of these tilting angles.

Table 2. Pore Angle ω (As Defined in Figure 3) and the Angle χ Being the Average of the Two Dihedral Angles $V-O_{ca}-C_{ca}-C_{pc}$ for the Different Structures[a]

phase	crystal system	ω (deg)	χ (deg)	α (deg)	deviation planarity biphenyl (deg)
np (empirical)[b]	monoclinic	42.0	143.7	84.4	0.9
np (calcd)	orthorhombic	27.2	142.5	84.5	46.3
lp (empirical)[c]	orthorhombic	78.6			
lp (calcd)	orthorhombic	86.9	165.5	87.5	46.7
lp (exptl)[d]	orthorhombic	87.6	164.1	80.6	1.9
np′ (calcd)	orthorhombic	147.5	139.6	85.8	49.1

[a] For the atomic labeling, see Figure S7 in the Supporting Information. α stands for the angle $O_{ca,1}-V-O_{ca,3}$ in the equatorial plane of the four carboxyl oxygens coordinated with V. The deviation from planarity is the angle between the planes of the two phenyl groups within the biphenyl linker. [b] Empirically determined based on synchrotron XRPD pattern with 7.5 bar of CO_2 pressure at 233 K. [c] Empirically determined based on synchrotron XRPD pattern with 15 bar CO_2 pressure at 233 K. [d] Determined based on the crystal data obtained from Rietveld structure refinement on laboratory XRPD pattern of COMOC-2(*lp*) at 293 K.

In complete agreement with the earlier work of Walker et al.,[34] addition of dispersion corrections[27,35] is needed to get realistic energy differences between the *lp* and *np* forms. Without dispersion interactions, the three minima are not found. As frequency calculations were performed for every point along the profile, we were able to determine also the vibrational entropic contributions of the smallest unit cell and to plot the free energy profiles for various temperatures. The numerical results reveal that the free energy barrier for the *lp* → *np* phase transition is more or less constant with temperature, with a value varying between 36 and 43 kJ mol^{-1} (Table 3).

Table 3. Free Energy Barriers ($\Delta G^{\ddagger}$ (*lp* → *np*) and $\Delta G^{\ddagger}$ (*lp* → *np*′) in kJ mol^{-1} Required for the Shape Transformations

temperature (K)	$\Delta G^{\ddagger}$ (*lp* → *np*)	$\Delta G^{\ddagger}$ (*lp* → *np*′)
0	37.9	39.8
50	37.6	39.4
150	36.5	38.6
250	36.6	39.4
350	38.3	41.7
500	40.7	45.2
650	43.1	48.7

The free energy difference between the *np* forms decreases from 38.3 to 27.2 kJ mol^{-1} when increasing the temperature from 0 to 650 K. The theoretically determined free energy profiles of the empty host give evidence for a tristable behavior of COMOC-2(V^{IV}), favoring the large pore structure when temperature rises. Experimentally, the breathing behavior is only observed at a certain CO_2 pressure. No phase transitions have taken place with CH_4. The occurrence of a breathing behavior depends on the strength of the host−guest interactions. For a molecule such as CO_2 exhibiting strong interactions with the pore walls, the free energy barrier toward the *np* may already be overcome at 1 bar, as demonstrated by the experiment. As our simulations were performed without guest molecules, we cannot correlate exactly the pore angle and lattice parameters for the *np* and *lp* shapes with the experimental values given in Table 1. In particular, the theoretical lattice parameter along the *c*-axis for the *np* form is smaller compared to the experimental value, since the *np* form may not fully close due to the presence of adsorbate molecules. Our simulations do however clearly show that COMOC-2(V^{IV}) has an intrinsic tristable behavior.

■ CONCLUSIONS

In conclusion, a V^{IV} carboxylate MOF COMOC-2 having the same framework topology as MIL-47 was synthesized and fully characterized. Unlike MIL-47, COMOC-2(V^{IV}) shows a breathing effect upon gas and vapor sorption at mild conditions. Similar to MIL-53, the sorption isotherms of CO_2 and CH_4 display a different shape at specific temperatures. Compared to COMOC-2(V^{IV}), COMOC-2(V^{III}/V^{IV}) increases the difficulty in triggering the flexibility of the framework. The theoretically determined free energy profile along the pore angle points toward a tristable behavior of the material. Apart from a regular *np* form, an overstretched narrow pore configuration was theoretically found. Future work will focus on the understanding of the phase transitions induced within COMOC-2(V^{IV}) by various other adsorbates, targeting potential applications in selective gas adsorption and molecular sensing.

■ ASSOCIATED CONTENT

Ⓢ Supporting Information

Crystallographic information file (CIF) of COMOC-2(*lp*), general information on the determination of the free energy profile, detailed XPS data analysis, TGA, Rietveld refinement plot, powder XRD measurements, and structural information from the ab initio calculations. This material is available free of charge via the Internet at http://pubs.acs.org.

■ AUTHOR INFORMATION

Corresponding Author

*E-mail: pascal.vandervoort@ugent.be.

Notes

The authors declare no competing financial interest.

■ ACKNOWLEDGMENTS

The ESRF is acknowledged for providing access to the Swiss−Norwegian Beamline. The authors acknowledge the financial support from the Ghent University BOF Grants 01P02911T and 01D31608, GOA Grant 01G00710, the Long Term Structural Methusalem Grant 01M00409, BELSPO in the frame of IAP 6/27, and the European Research Council (FP7(2007-2013) ERC Grant 240483. Computational resources (Stevin Supercomputer Infrastructure) and services were provided by Ghent University. Sumit Sachdeva and Canan Gücüyener (TUDelft) are gratefully acknowledged for the XPS analysis and N2 adsorption isotherms, respectively.

■ REFERENCES

(1) (a) Denayer, J. F. M.; Finsy, V.; Ma, L.; Alaerts, L.; De Vos, D. E.; Baron, G. V. *Microporous Mesoporous Mater.* **2009**, *120*, 221. (b) Trens, P.; Trung, T. K.; Tanchoux, N.; Bourrelly, S.; Llewellyn, P. L.; Loera-Serna, S.; Serre, C.; Loiseau, T.; Fajula, F.; Ferey, G. *J. Am. Chem. Soc.* **2008**, *130*, 16926. (c) De Weireld, G.; Hamon, L.; Serre, C.; Devic, T.; Loiseau, T.; Millange, F.; Ferey, G. *J. Am. Chem. Soc.* **2009**, *131*, 8775. (d) Rosi, N. L.; Eckert, J.; Eddaoudi, M.; Vodak, D. T.; Kim, J.; O'Keeffe, M.; Yaghi, O. M. *Science* **2003**, *300*, 1127. (e) Tonigold, M.; Lu, Y.; Mavrandonakis, A.; Puls, A.; Staudt, R.; Möllmer, J.; Sauer, J.; Volkmer, D. *Chem.—Eur. J.* **2011**, *17*, 8671.

(2) (a) Barthelet, K.; Marrot, J.; Riou, D.; Ferey, G. *Angew. Chem., Int. Ed.* **2001**, *41*, 281. (b) Ferey, G.; Serre, C. *Chem. Soc. Rev.* **2009**, *38*, 1380.

(3) Uemura, K.; Kitagawa, S.; Kondo, M.; Fukui, K.; Kitaura, R.; Chang, H. C.; Mizutani, T. *Chem.—Eur. J.* **2002**, *8*, 3586.

(4) Horike, S.; Shimomura, S.; Kitagawa, S. *Nat. Chem.* **2009**, *1*, 695.

(5) (a) Loiseau, T.; Serre, C.; Huguenard, C.; Fink, G.; Taulelle, F.; Henry, M.; Bataille, T.; Ferey, G. *Chem.—Eur. J.* **2004**, *10*, 1373. (b) Serre, C.; Millange, F.; Thouvenot, C.; Nogues, M.; Marsolier, G.; Louer, D.; Ferey, G. *J. Am. Chem. Soc.* **2002**, *124*, 13519. (c) Whitfield, T. R.; Wang, X. Q.; Liu, L. M.; Jacobson, A. J. *Solid State Sci.* **2005**, *7*, 1096. (d) Jacobson, A. J.; Vougo-Zanda, M.; Huang, J.; Anokhina, E.; Wang, X. Q. *Inorg. Chem.* **2008**, *47*, 11535. (e) Anokhina, E. V.; Vougo-Zanda, M.; Wang, X. Q.; Jacobson, A. J. *J. Am. Chem. Soc.* **2005**, *127*, 15000. (f) Mowat, J. P. S.; Miller, S. R.; Slawin, A. M. Z.; Seymour, V. R.; Ashbrook, S. E.; Wright, P. A. *Microporous Mesoporous Mater.* **2011**, *142*, 322.

(6) (a) Serre, C.; Bourrelly, S.; Vimont, A.; Ramsahye, N. A.; Maurin, G.; Llewellyn, P. L.; Daturi, M.; Filinchuk, Y.; Leynaud, O.; Barnes, P.; Ferey, G. *Adv. Mater.* **2007**, *19*, 2246. (b) Liu, Y.; Her, J. H.; Dailly, A.; Ramirez-Cuesta, A. J.; Neumann, D. A.; Brown, C. M. *J. Am. Chem. Soc.* **2008**, *130*, 11813. (c) Thallapally, P. K.; Tian, J.; Kishan, M. R.; Fernandez, C. A.; Dalgarno, S. J.; McGrail, P. B.; Warren, J. E.; Atwood, J. L. *J. Am. Chem. Soc.* **2008**, *130*, 16842. (d) Trung, T. K.; Trens, P.; Tanchoux, N.; Bourrelly, S.; Llewellyn, P. L.; Loera-Serna, S.; Serre, C.; Loiseau, T.; Fajula, F.; Ferey, G. *J. Am. Chem. Soc.* **2008**,

130, 16926. (e) Volkringer, C.; Loiseau, T.; Guillou, N.; Ferey, G.; Elkaim, E.; Vimont, A. *Dalton Trans.* **2009**, 2241.

(7) Bourrelly, S.; Llewellyn, P. L.; Serre, C.; Millange, F.; Loiseau, T.; Ferey, G. *J. Am. Chem. Soc.* **2005**, *127*, 13519.

(8) (a) Wang, Z. Q.; Cohen, S. M. *J. Am. Chem. Soc.* **2009**, *131*, 16675. (b) Ramsahye, N. A.; Trung, T. K.; Bourrelly, S.; Yang, Q. Y.; Devic, T.; Maurin, G.; Horcajada, P.; Llewellyn, P. L.; Yot, P.; Serre, C.; Filinchuk, Y.; Fajula, F.; Ferey, G.; Trens, P. *J. Phys. Chem. C* **2011**, *115*, 18683. (c) Biswas, S.; Ahnfeldt, T.; Stock, N. *Inorg. Chem.* **2011**, *50*, 9518.

(9) Leclerc, H.; Devic, T.; Devautour-Vinot, S.; Bazin, P.; Audebrand, N.; Ferey, G.; Daturi, M.; Vimont, A.; Clet, G. *J. Phys. Chem. C* **2011**, *115*, 19828.

(10) Yot, P. G.; Ma, Q.; Haines, J.; Yang, Q.; Ghoufi, A.; Devic, T.; Serre, C.; Dmitriev, V.; Ferey, G.; Zhong, C.; Maurin, G. *Chem. Sci.* **2012**, *3*, 1100−1104.

(11) (a) Finsy, V.; Kirschhock, C. E. A.; Vedts, G.; Maes, M.; Alaerts, L.; De Vos, D. E.; Baron, G. V.; Denayer, J. F. M. *Chem.—Eur. J.* **2009**, *15*, 7724. (b) Finsy, V.; Ma, L.; Alaerts, L.; De Vos, D. E.; Baron, G. V.; Denayer, J. F. M. *Microporous Mesoporous Mater.* **2009**, *120*, 221. (c) Couck, S.; Denayer, J. F. M.; Baron, G. V.; Remy, T.; Gascon, J.; Kapteijn, F. *J. Am. Chem. Soc.* **2009**, *131*, 6326. (d) De Vos, D. E.; Maes, M.; Vermoortele, F.; Alaerts, L.; Couck, S.; Kirschhock, C. E. A.; Denayer, J. F. M. *J. Am. Chem. Soc.* **2010**, *132*, 15277. (e) Denayer, J. F. M.; Couck, S.; Remy, T.; Baron, G. V.; Gascon, J.; Kapteijn, F. *Phys. Chem. Chem. Phys.* **2010**, *12*, 9413.

(12) Serra-Crespo, P.; van der Veen, M. A.; Gobechiya, E.; Houthoofd, K.; Filinchuk, Y.; Kirschhock, C. E. A.; Martens, J. A.; Sels, B. F.; De Vos, D. E.; Kapteijn, F.; Gascon, J. *J. Am. Chem. Soc.* **2012**, *134*, 8314.

(13) (a) Serre, C.; Horcajada, P.; Maurin, G.; Ramsahye, N. A.; Balas, F.; Vallet-Regi, M.; Sebban, M.; Taulelle, F.; Ferey, G. *J. Am. Chem. Soc.* **2008**, *130*, 6774. (b) Horcajada, P.; Chalati, T.; Serre, C.; Gillet, B.; Sebrie, C.; Baati, T.; Eubank, J. F.; Heurtaux, D.; Clayette, P.; Kreuz, C.; Chang, J. S.; Hwang, Y. K.; Marsaud, V.; Bories, P. N.; Cynober, L.; Gil, S.; Ferey, G.; Couvreur, P.; Gref, R. *Nat. Mater.* **2010**, *9*, 172.

(14) (a) Llewellyn, P. L.; Maurin, G.; Devic, T.; Loera-Serna, S.; Rosenbach, N.; Serre, C.; Bourrelly, S.; Horcajada, P.; Filinchuk, Y.; Ferey, G. *J. Am. Chem. Soc.* **2008**, *130*, 12808. (b) Boutin, A.; Springuel-Huet, M. A.; Nossov, A.; Gedeon, A.; Loiseau, T.; Volkringer, C.; Ferey, G.; Coudert, F. X.; Fuchs, A. H. *Angew. Chem., Int. Ed.* **2009**, *48*, 8314. (c) Devautour-Vinot, S.; Maurin, G.; Henn, F.; Serre, C.; Devic, T.; Ferey, G. *Chem. Commun.* **2009**, 2733. (d) Yang, C.; Wang, X. P.; Omary, M. A. *Angew. Chem., Int. Ed.* **2009**, *48*, 2500. (e) Boutin, A.; Couck, S.; Coudert, F. X.; Serra-Crespo, P.; Gascon, J.; Kapteijn, F.; Fuchs, A. H.; Denayer, J. F. M. *Microporous Mesoporous Mater.* **2011**, *140*, 108.

(15) Senkovska, I.; Hoffmann, F.; Froba, M.; Getzschmann, J.; Bohlmann, W.; Kaskel, S. *Microporous Mesoporous Mater.* **2009**, *122*, 93.

(16) Lasocha, W.; Lewinski, K. *J. Appl. Crystallogr.* **1994**, *27*, 437.

(17) Petricek, V.; Dusek, M.; ; Palatinus, L. *Jana2006: The Crystallographic Computing System*; 2006.

(18) Hammersley, A. P. ESRF Internal Report.

(19) Boultif, A.; Louer, D. *J. Appl. Crystallogr.* **1991**, *24*, 987.

(20) STOE & CIE GmBH. *STOE WinXPOW*, version 2.11.

(21) Walker, A. M.; Civalleri, B.; Slater, B.; Mellot-Draznieks, C.; Cora, F.; Zicovich-Wilson, C. M.; Roman-Perez, G.; Soler, J. M.; Gale, J. D. *Angew. Chem., Int. Ed.* **2010**, *49*, 7501.

(22) Stavitski, E.; Pidko, E. A.; Couck, S.; Remy, T.; Hensen, E. J. M.; Weckhuysen, B. M.; Denayer, J.; Gascon, J.; Kapteijn, F. *Langmuir* **2011**, *27*, 3970.

(23) Triguero, C.; Coudert, F. X.; Boutin, A.; Fuchs, A. H.; Neimark, A. V. *J. Phys. Chem. Lett.* **2011**, *2*, 2033.

(24) (a) Kresse, G.; Furthmuller, J. *Phys. Rev. B* **1996**, *54*, 11169. (b) Kresse, G.; Furthmuller, J. *Comput. Mater. Sci.* **1996**, *6*, 15. (c) Kresse, G.; Hafner, J. *Phys. Rev. B* **1993**, *47*, 558. (d) Kresse, G.; Hafner, J. *Phys. Rev. B* **1994**, *49*, 14251.

(25) (a) Perdew, J. P.; Burke, K.; Ernzerhof, M. *Phys. Rev. Lett.* **1996**, *77*, 3865. (b) Perdew, J. P.; Burke, K.; Ernzerhof, M. *Phys. Rev. Lett.* **1997**, *78*, 1396.

(26) Blochl, P. E. *Phys. Rev. B* **1994**, *50*, 17953.

(27) Grimme, S. *J. Comput. Chem.* **2006**, *27*, 1787.

(28) Henkelman, G.; Uberuaga, B. P.; Jonsson, H. *J. Chem. Phys.* **2000**, *113*, 9901.

(29) Ghysels, A.; Verstraelen, T.; Hemelsoet, K.; Waroquier, M.; Van Speybroeck, V. *J. Chem. Inf. Model.* **2010**, *50*, 1736.

(30) Spek, A. *J. Appl. Crystallogr.* **2003**, *36*, 7.

(31) Serra-Crespo, P.; Gobechiya, E.; Ramos-Fernandez, E. V.; Juan-Alcañiz, J.; Martinez-Joaristi, A.; Stavitski, E.; Kirschhock, C. E. A.; Martens, J. A.; Kapteijn, F.; Gascon, J. *Langmuir* **2012**, *28*, 12916.

(32) Neimark, A. V.; Coudert, F. X.; Boutin, A.; Fuchs, A. H. *J. Phys. Chem. Lett.* **2010**, *1*, 445.

(33) Llewellyn, P. L.; Horcajada, P.; Maurin, G.; Devic, T.; Rosenbach, N.; Bourrelly, S.; Serre, C.; Vincent, D.; Loera-Serna, S.; Filinchuk, Y.; Ferey, G. *J. Am. Chem. Soc.* **2009**, *131*, 13002.

(34) Walker, A. M.; Civalleri, B.; Slater, B.; Mellot-Draznieks, C.; Corà, F.; Zicovich-Wilson, C. M.; Román-Pérez, G.; Soler, J. M.; Gale, J. D. *Angew. Chem., Int. Ed.* **2010**, *49*, 7501.

(35) (a) Grimme, S. *J. Comput. Chem.* **2004**, *25*, 1463. (b) Grimme, S.; Antony, J.; Ehrlich, S.; Krieg, H. *J. Chem. Phys.* **2010**, *132*, 154104.